



Liu, D., & Flewitt, P. (2017). Deformation and fracture of carbonaceous materials using *in situ* micro-mechanical testing. *Carbon*, 114, 261–274. <https://doi.org/10.1016/j.carbon.2016.11.084>

Peer reviewed version

Link to published version (if available):
[10.1016/j.carbon.2016.11.084](https://doi.org/10.1016/j.carbon.2016.11.084)

[Link to publication record in Explore Bristol Research](#)
PDF-document

This is the accepted author manuscript (AAM). The final published version (version of record) is available online via Elsevier at DOI: 10.1016/j.carbon.2016.11.084. Please refer to any applicable terms of use of the publisher.

University of Bristol - Explore Bristol Research

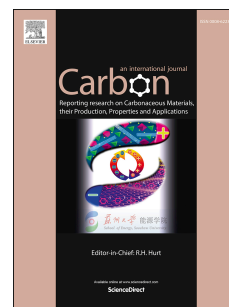
General rights

This document is made available in accordance with publisher policies. Please cite only the published version using the reference above. Full terms of use are available:
<http://www.bristol.ac.uk/red/research-policy/pure/user-guides/ebr-terms/>

Accepted Manuscript

Deformation and fracture of carbonaceous materials using *in situ* micro-mechanical testing

Dong Liu, Peter E.J. Flewitt



PII: S0008-6223(16)31069-7

DOI: [10.1016/j.carbon.2016.11.084](https://doi.org/10.1016/j.carbon.2016.11.084)

Reference: CARBON 11523

To appear in: *Carbon*

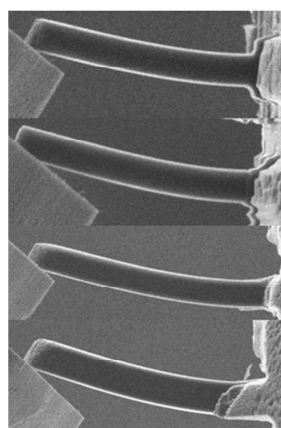
Received Date: 16 September 2016

Revised Date: 28 November 2016

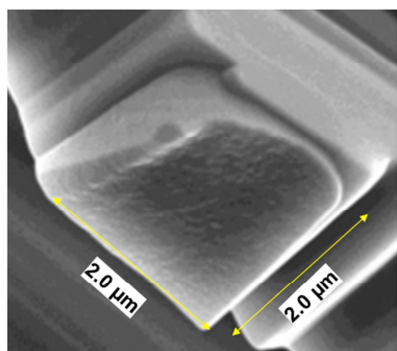
Accepted Date: 30 November 2016

Please cite this article as: D. Liu, P.E.J. Flewitt, Deformation and fracture of carbonaceous materials using *in situ* micro-mechanical testing, *Carbon* (2017), doi: 10.1016/j.carbon.2016.11.084.

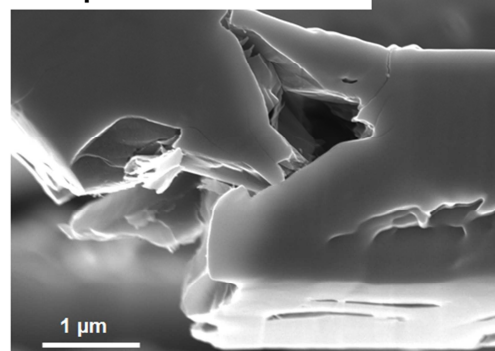
This is a PDF file of an unedited manuscript that has been accepted for publication. As a service to our customers we are providing this early version of the manuscript. The manuscript will undergo copyediting, typesetting, and review of the resulting proof before it is published in its final form. Please note that during the production process errors may be discovered which could affect the content, and all legal disclaimers that apply to the journal pertain.



Vitreous carbon:
brittle fracture



Nuclear graphite:
complex fracture mode



Deformation and fracture of carbonaceous materials using *in situ* micro-mechanical testing

Dong Liu*¹ and Peter E J Flewitt

HH Wills Physics Laboratory, University of Bristol, Tyndall Avenue, BS8 1TL

Abstract

The local mechanical properties of vitreous carbon and another three porous graphite materials have been investigated using a novel *in situ* micro-cantilever bending approach. Vitreous carbon is used for validation of the micro-mechanical measurements. Filter graphite is a single phase material with ~52 vol.% porosity. Gilsocarbon graphite is a nuclear-grade graphite that is currently used in the advanced gas-cooled reactors in the UK with ~20 vol.% porosity in the filler particles and matrix; Pile Grade-A graphite (PGA) was extracted from a fuel brick within a Magnox reactor core with 15% weight loss due to neutron irradiation and CO₂ radiolytic oxidation. The ‘true’ material properties obtained at micro-scale are found to be of much higher value than those measured at the macro-scale due to different failure controlling mechanisms. In particular for the PGA graphite, the micro-mechanical tests allowed the mechanical properties of the filler particles and matrix to be measured separately. The filler particles showed a higher stiffness and flexural strength compared with the matrix indicating the different influence of neutron irradiation on these two constituents. It is demonstrated here that the local mechanical properties of carbonaceous materials with various complex microstructures and even following neutron irradiation can be successfully evaluated.

1. Introduction

Carbon has many allotropic forms of which several are used for a wide range of engineering applications. Of these forms those most often encountered are diamond and graphite; these two are the allotropes that can be completely characterised. Another form is non-graphitizing vitreous carbon derived from pitches and polymeric precursors or produced by various modern thin film deposition and growth techniques [1]. There are several interpretations of the detailed atomic structure of this class of material, but as shown by Harris [2] the final arrangement is conditional upon the fabrication route adopted. Vitreous carbon has physical properties and fracture characteristics similar to glass and ceramic materials, and one particular application is in the form of a reticulated foam. Its good bio-compatibility with

* Corresponding author. Tel: 01865 283326; Email: dong.liu@materials.ox.ac.uk
Present address: Department of Materials, University of Oxford, Parks Road, Oxford OX1 3PH.

blood and tissue enabled the applications for medical technology and biotechnology [3]. By comparison, there are a range of industrial graphites [4], many of which are polygranular, aggregate materials prepared by essentially heating a mixture of coke particles and pitch binder in the absence of air to temperatures of up to 3000°C. One particular example for the application of these graphites is as a moderator and structural supports within the reactor core of UK gas-cooled civil nuclear power plants. These nuclear-grade graphites are electro-graphites produced by modifications to conventional graphite manufacturing methods, with special care being taken to exclude high-cross section impurities such as boron [5]. It has been long recognised that neutron irradiation produces large changes in the elastic modulus and strength of single crystal and polygranular graphites [5][6][7]. The effects of atomic displacements in graphite arising from collisions with fast neutrons lead to the accumulation of damage at various exposure temperatures. The induced lattice defects are based upon point defects, Frenkel pairs, which alter both physical and mechanical properties of the graphite. During these processes energy is stored within the graphite. To date, when addressing the effect of neutron irradiation on the mechanical properties and fracture characteristics of UK reactor core graphites, attention has focussed on the role of bulk macroscopic mechanical and thermal properties and dimensional changes [6]. The measurements made on macro-size samples removed periodically from reactors, either by trepanning from bricks or surveillance schemes, have not allowed deconvolution of the neutron irradiation damage from the radiolytic oxidation induced porosity contribution to the mechanical properties of the constituent phases, namely filler particles and binder matrix. It would be instructive to have a measure of the changes introduced to individual components of the complex polygranular aggregate microstructure of these graphites.

Micro-mechanical testing has been used to characterise the mechanical properties of materials for a wide range of applications, such as micro-electro-mechanical systems [8][9], single crystal and polycrystalline silicon and silicon-based dielectric thin films [10][11][12][13], tungsten-based alloys for the use of plasma-facing components in future magnetic confinement fusion reactors [14], nanocrystalline metals [15], and in biomaterials to test constituent elements such as individual collagen fibrils [16]. Amongst the micro-scale approaches, nano-indentation tests provides the hardness and indentation modulus on the surface of samples; but the geometry of the elastic/inelastic zone below the indenter varies with crystal orientation and local microstructure. Since the stress state within that volume is complex, this hinders interpretation of the test results. For some materials such as nuclear

graphites, nano-indentation is susceptible to localised microstructural inhomogeneity and surface roughness [17]. Another approach is to create a micro-scale specimen, typically using techniques such as focus ion beam milling [10][18], micro-electron-discharge machining and laser ablation, and then deform the specimens by a non-sharp tip nano-indenter such as a conical or flat punch that has a large diameter compared with the local microstructure, or a purpose-built loading probe [19]. The tests can be undertaken either *ex situ* under an optical microscope [11] or *in situ* within a scanning electron microscope [10] and/or an atomic force microscope [12]. A range of test geometries have been adopted including pillar compression, single cantilever bending, clamped cantilever bending, double cantilever bending and uniaxial tension [19][18][10]. For the two most commonly used configurations, pillar compression specimens have a length to diameter ratio of 2 to 2.5 : 1 [18] and single cantilever bending specimens usually with a length to width aspect ratio larger than four [11][19][10]. In these cases, the specimen manufacture process is more complicated than that adopted for conventional nano-indentation, but it is possible to obtain a measure of elastic modulus, yield, tensile and flexural strength, fracture toughness and fracture energy, e.g. by introducing a Chevron notch using low-current focus ion beam line milling [12].

There is often a requirement to undertake micro-mechanical measurements of the deformation and fracture properties of carbonaceous materials because of (i) the form of the material such as a porous foam [20]; (ii) the need to evaluate specific features of the microstructure; or (iii) the need to minimise the active volume of materials previously exposed to neutron irradiation [21][7]. Approaches focussed on reducing the size of the irradiated test specimens give rise to a range of miniaturised specimens tested using different geometrical arrangements. In the specific case of irradiated nuclear graphites, smaller length-scale tests, such as the mm-scale Brazilian disc geometry test, have been adopted by Heard et al. [22]. However, the latter authors provided only final failure load for the one macroscopic graphite specimen tested [22]. By adopting focussed ion beam milling, it has been possible to explore a wide range of micro-scale geometry specimens that have been tested to measure mechanical properties [19][23][15][10][18]. One of the first applications that invoked gallium ion milling to prepare irradiated graphite specimens in a focussed ion beam (FIB) workstation and then conducting an *in situ* trench-probe test, was described by Heard et al [22]. During that particular test, the specimen was moved towards a fixed probe, the localised fracture of irradiated PGA graphite was observed but no outputs of load or displacement were provided. Recently, a quantitative approach adopting micro-scale cantilever beam geometry

unirradiated nuclear graphite, prepared and tested within a Dualbeam workstation that contains a force measurement system, has been developed by Liu et al [23]. This approach is able to produce a measure of stress-strain (force-displacement), elastic modulus, fracture strength and *in situ* characterisation of the progressive development of damage.

Several challenges remain for evaluating the mechanical properties of carbonaceous materials. The first is to ensure that representative mechanical properties measured are appropriate over a range of length-scale. In the case of commercial graphites which have microstructures with varying degrees of complexity, it is necessary to establish if micro-scale tests provide a measure of mechanical properties and fracture characteristics similar to those obtained at the macro-length scale. The latter length-scale is typical of data obtained from conventional laboratory tests. It is therefore important to perform tests at the micro-length-scale to evaluate the mechanical properties and fracture characteristics of specific microstructural constituents of commercial graphites, for example the polygranular graphite used in the core of AGR gas-cooled reactors in the UK. The second is that it is necessary to understand how the properties of the constituent phases change when subject to hostile environments such as those encountered during service in UK gas-cooled nuclear power stations, namely hot CO₂ gas and fast neutron irradiation. As a consequence, we consider a method for producing and undertaking measurements using micro-length-scale cantilever test specimens. Four carbonaceous materials have been selected to address the specific challenges described above. The first is a vitreous carbon that has a linear-elastic response and known material properties at the macro-length-scale. This material has been adopted to establish if the micro-scale mechanical properties and fracture characteristics are representative of macro-scale data. The second material has a microstructure intermediate between the simple linear-elastic vitreous carbon and the complex commercial graphites. A filter graphite with a large volume fraction of macro-porosity to allow evaluation of the micro-scale properties of the graphite without a contribution from the macro-pores. It is the overall microstructure, graphite plus porosity, measured at the macro-scale that is known to contribute to the quasi-brittle characteristics of this material. Finally, two commercial graphites used in the reactor cores of UK gas-cooled power stations have been selected: Gilsocarbon graphite and Pile Grade A, PGA, graphite. These have been tested to establish if it is possible to provide a measure of the mechanical properties of the respective graphitised Gilsonite and needle coke filler particles and the associated binder matrix. In addition, similar measurements have been made on PGA graphite post neutron irradiation in a hot CO₂ gas environment to demonstrate the benefits of

evaluating mechanical properties using small volumes of active material to provide necessary data for input to multi-scale computer models.

In this paper, we describe in Section 2 the experimental detail including a method for producing micro-length-scale cantilever beam specimens and the four selected carbonaceous materials. The mechanical properties measured and the associated fracture characteristics are discussed in Section 3 and Section 4. In the case of the neutron irradiated specimens, the change of local mechanical properties for the filler particles and binder phase have been explored and general conclusions are drawn in Section 5.

2. Experiments

2.1 The materials

Four types of materials have been studied, Table 1. Vitreous carbon is a glassy material with a low degree of crystallographic order. The material studied here was supplied with millimetre size ligaments (1 mm width by 2 mm in length) removed from a foam structure (10 pore per inch), Fig. 1a; the properties of interest are listed in Table I.

Table I Material physical and mechanical properties [1, 6, 25, 26, 27, 28, 29]*

	Apparent bulk density (g/cm ³)	Porosity vol.%	Bulk E (GPa)	Bulk flexural strength (MPa)	Compressive strength (MPa)
Vitreous carbon	1.42-1.54	0 or ≤ 0.05	20-35	120-400	450-1000
PG25 graphite	1.05	~52	0.2-0.3	3.0-5.2	6.0-9.0
Gilsocarbon graphite	1.81	~20	11.0-12.0	20 to 30	70 to 80
Pile Grade-A graphite	1.74	~20	10-12 Parallel*; 5-6 Perpendicular*;	12-20 Parallel*; 9-14 perpendicular*;	25-30

* Parallel refers to the measurements undertaken along the direction of extrusion; perpendicular refers to measurements normal to the direction of extrusion for PGA graphite.

The filter graphite material (PG25) studied was manufactured by Morganite Electrical Carbon Ltd. Here the material contains interconnected macro-pores generated by manufacturing, Fig. 1b. These macro-pores have been characterised by computed X-ray tomography using a Nikon Metrology 225/320 kV Custom Bay system (Manchester University, UK) with a voxel size of $16.4 \times 16.4 \times 16.4 \mu\text{m}$ on a sample of $20 \times 20 \times 22 \text{ mm}$ - a reconstructed image of the 3D structure is shown in Fig. 1c. The results showed a total porosity of $42.8 \pm 0.5 \text{ vol.}\%$ that is fully interconnected (99.9% of the total porosity is one

open pore). In addition, micro-pores in the matrix were observed by three-dimensional high resolution focussed Ga^+ ion beam serial milling tomography in a Helios NanoLab 600i Dualbeam workstation, Fig. 1d. The measurement at several locations indicated an average micro-scale porosity of 16 ± 2 vol.% with pore size ranging from $0.05 \mu\text{m}$ to $2 \mu\text{m}$ (equivalent sphere diameter), Fig. 1d. Therefore, the total volume of the pores in this PG25 graphite is approximately $42.8 \text{ vol.\%} + 16 \text{ vol.\%} \times (1 - 42.8 \text{ vol.\%}) = 52 \text{ vol.\%}$. The typical macro-mechanical properties are listed in Table I.

The Gilsocarbon graphite studied was a moulded medium-grained IM1-24 (GCMB grade) polygranular nuclear graphite supplied by EDF Energy Ltd (manufactured by Graftech). It comprised spherical Gilsonite (a naturally occurring solid hydrocarbon bitumen) filler particles of $\sim 0.5 \text{ mm}$ dia. in a coal-tar pitch binder matrix, Fig. 2a. It is used as fast neutron moderator and structural component in the core of the UK Advanced Gas-cooled Reactor (AGR) fleet. This IM1-24 graphite is nearly isotropic (anisotropic ratio of 1:1.1) with the bulk elastic modulus in the range of 11 to 12 GPa, depending on the orientation, and the tensile strength between 19 to 20 MPa. The total porosity is considered to be 20 vol.%; macro-pores are measured to be 4 to 6 area% ($10 \mu\text{m}$ to $200 \mu\text{m}$ equivalent circle diameter) from optical and SEM images. The data for the macro-pores have been further confirmed by computed X-ray tomography scans on a cube sample of $20 \times 20 \times 20 \text{ mm}$ using the same equipment for PG25 graphite with a resolution of $15.8 \times 15.8 \times 15.8 \mu\text{m}$: the measured porosity was about $6.9 \pm 0.4 \text{ vol.\%}$, Fig. 2b. At this resolution, the pores measured were mainly isolated which is different from PG25 graphite. Both 2D optical and 3D tomography approaches indicate that the macro-pores represent a small part of the total porosity. The micro-pores contained in the filler particles and matrix were measured by high resolution serial sectioning tomography using the same approach as for PG25. Example slices of the cross-sections located inside the matrix (site 1), at the outer-region of the filler particles (site 2 for 'onion skin'), and near to the centre of the filler particles (site 3), Fig. 2a. The size of the pores at three sites range from $0.04 \mu\text{m}$ to $2 \mu\text{m}$ (equivalent sphere diameter), and occupy 13 to 15 vol.% of the total volume.

Pile Grade-A provided by Magnox Ltd is another grade of nuclear graphite used in Magnox reactors. PGA contains large elongated filler particles (0.1 to 1.0 mm in length) made from highly crystalline porous petroleum needle coke (by-product of oil refining process), and the crystallographic basal planes tend to lie parallel to extrusion axis as a result of processing. These filler particles are embedded in a coal tar pitch binder plus ground coke flour matrix. As-

manufactured material has a porosity of ~20 vol.% comprising both macro-pores and micro-pores distributed within the matrix, Fig. 3a, and the filler particles, Fig. 3b. In particular, the filler particles contains elongated micro-pores oriented along the extruded direction, Fig. 3b. The mechanical and physical properties of the PGA graphite vary with direction parallel to and perpendicular to the extrusion direction, Table I. In the present study, both unirradiated and irradiated PGA graphite have been investigated. The irradiated specimen was subjected to fast neutron irradiation ($33.200 \times 10^{20} \text{ n}\cdot\text{cm}^{-2}$ DIDO equivalent dose) and radiolytic oxidation in the CO_2 coolant gas at a temperature of 287°C with a weight loss of 15%.

Prior to micro-mechanical testing, X-ray diffraction (XRD) for the vitreous carbon, PG25 graphite, IM1-24 and PGA graphite samples was carried out using a X'PERT PRO diffractometer with a $\text{CuK}\alpha$ source. Each scan covers a 2θ range from 5° to 140° at a step size of 0.02 deg and a dwell time of 1.5s per step. The $K_{\alpha 1}$ wavelength used for d-spacing calculation was 0.15405 nm, and overlays of diffraction patterns for the four materials are shown in Fig. 4a. Overall, the calculated {002} lattice space for filter graphite is about 0.337 nm ({004} is about 0.168 nm), 0.338 nm for IM1-24 graphite ({004} is about 0.169 nm). For the PGA these values are {002} and {004} 0.331 and 0.156 nm, respectively. For vitreous carbon, the diffraction pattern is degraded and consistent with that obtained from low degree of order associated with glassy materials, Fig. 4a. In addition, Raman spectroscopy measurements using a Reinshaw Ramascope model 2000 with a laser source of 632.8 nm was applied to the same samples. An example of overlaid spectra are shown in Fig. 4b indicating the existence of graphite crystallites (G peak) and disorder (D, D' and D*); only spectra for three materials are shown here as PGA graphite has similar spectrum to IM1-24 graphite. For PG25, similar forms of carbon were observed as Gilsocarbon graphite. The vitreous carbon foam has mainly a disordered structure consistent with XRD measurements.

2.2 *In situ* micro-cantilever tests

The approach adopted is an *in situ* force measurement system installed on a micro-manipulator in a Helios NanoLab 600i Dualbeam workstation - it is a similar approach as described in ref. [19, 29]. Step I was to mill two trenches (the size of the trench is usually the length of the expected cantilever, h , 15 to 20 μm , by a depth more than 10 μm) at 45° into the edge of the bulk material, Fig. 5a. For this step a beam energy of 30 keV and current of 6.5 nA was selected. The two trenches were usually separated by a wall with a thickness of about three times of the section size of the final cantilever, d . Step II was to mill two trenches from the other side of the sample using the same current and voltage settings, Fig. 5b. After these

two steps, a cantilever of $3d \times 3d \times h$ was produced. The beam current was reduced progressively from 2.7 nA to 96 pA to reduce the cantilever size to the final dimension $d \times d \times h$ and minimise the Ga^+ damage at the surface. A modified force measurement probe controlled by a micro-manipulator (Kleindiek Nanotechnik GmbH) installed in the Dualbeam workstation was used to load the cantilevers; the entire loading process was programmed to be displacement-controlled ($0.025 \mu\text{m} \cdot \text{s}^{-1}$). The advantage of this approach is that the deformation and fracture of the specimens can be viewed and recorded using SEM imaging. To generate load-displacement curves, the coordinates of the loading point were extracted manually from the images at a certain load. The elastic modulus was then determined from the linear part of the load-displacement curve and the flexural strength from the maximum load at fracture, the loading configuration and the specimen geometry. Prior to each test, the loading probe was calibrated against a standard provided by the manufacture to derive the spring constant and the results validated using single crystal silicon of known orientation [19]. For the irradiated PGA graphite tests, certain irradiation protection procedure was adopted such as using an aluminium dish with a diameter of 105 mm to collect the debris. For each of the materials tested, a range of cantilever specimens with different cross-section sizes and lengths were made. However, the maximum load that could be applied by the loading probe was $360 \mu\text{N}$, and this sets a limit on the specimen size.

Errors associated with the present micro-cantilever beam test method mainly arise from two sources where the first relates to the determination of specimen displacement from the SEM images. To reduce this error, 10 measurements at a different magnification of the same image sequence have been undertaken to give a final average value. There was less than a 3 to 4 % standard deviation associated with the displacement for all the tests. The second was that the loading probe slides along the length of the cantilever during loading, which becomes pronounced at large displacements. Since elastic modulus was determined from the linear part of the load-displacement curve at a small displacement, the derived value was less affected. For the determination of the flexural strength, the loading arm length between the loading point and the fracture initiation site was measured from the last frame of the image to minimise this error. Cross-sections of the cantilever beams were measured at 10 different locations along the length for each specimen and was evaluated according to the fractured location. This ensured that the accuracy in the interpretation of the data was within 5%.

3. Results

3.1 Vitreous carbon

Four cantilever specimens were made and tested with the dimensions of $1.75 \times 1.75 \times 11.50 \mu\text{m}$, $1.25 \times 1.25 \times 8.80 \mu\text{m}$, $2.00 \times 2.00 \times 17.00 \mu\text{m}$ and $3.25 \times 3.25 \times 21.00 \mu\text{m}$, respectively, Fig. 6a. All the specimens showed a linear-elastic load-displacement curve followed by prompt fracture at the proportional limit, Fig. 6b. The fracture surface of the four specimens each displayed features typical of brittle fracture, Fig. 6b. The elastic modulus values fall between 25 to 35 GPa (mean 29 GPa) with no systematic change with the section size of the specimen over the range tested, Fig. 6c. Flexural strength was determined from $\sigma = FL/Z$ (σ : flexural strength (MPa), F : loading force (μN), L : loading arm length (μm); Z : section modulus of the cantilever cross-section). An average value of ~ 350 MPa was derived from the four specimens. The measured elastic modulus and corresponding flexural strength are listed in Table II. The failure strain centred around 1.0 to 1.8 % for this vitreous carbon material, and is similar to values obtained for pure pyrolytic carbon (1.28% to 1.58% [30], low temperature isotropic form of pyrolytic carbon (0.9-1.1%) [3], polycrystalline graphite (0.1 to 0.7%) [3].

3.2 Filter graphite (PG25)

Micro-cantilever specimens were milled from filter graphite PG25 and these contained sub-micro pores. When under loads $\leq 1/3$ of the fracture load, a linear load-unload response was observed, Fig. 7a. For loads above this range the displacement was non-linear and the post peak fracture was progressive, Fig. 7b, with clear load drops (marked as drop1, 2 and 3) as a main crack formed and propagated close to the root of the cantilever. The first drop of about $5 \mu\text{N}$ corresponds to a small crack formed parallel to the root (marked as crack1 in Fig. 7b). This is followed by a load increase of about $3 \mu\text{N}$ (as the peak load is approached), prior to the formation of a new large cross-sectional crack, crack2 in Fig. 7b. This leads to the closure of the previously formed crack as the local stress/strain was redistributed. As a consequence, the load dropped by about $10 \mu\text{N}$. Finally as this large crack propagated across the section the load dropped to nearly zero. These post-peak load drops and the associated crack propagation illustrates the progressive fracture behaviour within the material at the micro-scale. However, at this stage, (i) the fracture path was complex and difficult to quantify and (ii) the displacement was large and the direction of the applied load relative to the specimen had changed.

The geometry, load at fracture, elastic modulus and calculated flexural strength for the seven cantilevers tested are listed in Table II. For some of the specimens, multiple loading cycles were applied to obtain information on permanent set, see Table II. The average value for E was about 22 GPa with a standard deviation of 7.9 GPa. The lowest value measure was ~11 GPa and highest was ~35 GPa. The lower value corresponds to a cantilever specimen with significant pre-existing defects within the root region. The average flexural strength of all the cantilever specimens was 344 ± 160 MPa; the large scatter was consistent with the presence of defects contained within each individual cantilevers and the complex geometry of those defects. In terms of the measurement error associated with the flexural strength, it mainly originates from the pixel-based displacement measurement from the SEM images. Examination of the fracture surface of all specimens revealed that (i) the fracture surface usually comprised several steps as shown in Fig. 7c; and (ii) fracture occurred along the interfaces between crystallites at preferred locations with a complex 3D geometry.

3.3 IM1-24 graphite

IM1-24 graphite has filler particles bonded together by binder matrix. Compared with PG25 graphite, the microstructure is complex, Fig. 2. For some of the cantilever specimens, load-unload cycles were applied to acquire information on residual displacement on unloading, Fig. 8a. For loads greater than 50% of the failure load, permanent displacements were observed after unloading (after cycle 2 this was about $0.04 \mu\text{m}$; after cycle 3 this was about $0.08 \mu\text{m}$), Fig. 8a. However, the loading modulus of the cantilever remains approximately the same for each cycle, Table II. Overall, there is linear load-displacement at lower loads and non-linearity prior to final failure. Some of the cantilevers contained very complex arrangements of pre-existing defects and this resulted in intricate loading curves, Fig. 8b. In this particular case, a crack was formed at about two thirds of the peak load during load cycle 1, and this caused a reduction in the slope of the curve as more displacement was applied. Upon unloading, a permanent displacement was observed and the slope of the second loading cycle decreased to about $35.7 \mu\text{N}/\mu\text{m}$ compared with $43.0 \mu\text{N}/\mu\text{m}$ for cycle 1. During load cycle 2, a large crack was formed at about $30 \mu\text{N}$; this crack was associated with a load drop and formed at a different location from the previous pop-in in load cycle 1. Upon unloading, the cantilever did not return to the previous position, however, upon re-loading, load cycle three, the slope ($\sim 36.8 \mu\text{N}/\mu\text{m}$) remained nearly the same as for the previous cycle. Post-peak progressive failure was observed with load drops in both cycle 2 and cycle 3. This was a typical example of cantilever specimens that contained complex surface breaking defects and

the fracture was no longer abrupt brittle. In total, eight specimens were tested and the measured properties and loading cycles are listed in Table II. For comparison, E values are plotted in Fig. 8c as a function of specimen section size together with literature values for the macro-scale specimens. In general, values for E at micro-scale cluster between 10 and 30 GPa with some values extending to ~ 67 GPa. The flexural strength ranged from 73 MPa to 984 MPa at the micro-scale, Fig. 8d, which are much higher than the corresponding macro-scale values, see Table I and ref [31] (22.3 to 26.9 MPa). The large scatter at micro-scale can be attributed to the presence of micro-scale flaws and when their presence is minimal the measured properties approach the value for defect-free material.

3.4 PGA graphite

The PGA graphite samples studied in the present work included both as-manufactured and one removed from a reactor core brick following a period of in-service irradiation and radiolytic oxidation. The latter introduced changes to the microstructure and associated physical properties. In the unirradiated condition, the matrix has a surface morphology of randomly distributed flakes, Fig. 3a, and focussed ion beam milled cross-sections through the matrix revealed the presence of micro- and sub-micrometre pores, Fig. 3b. Following irradiation and radiolytic oxidation, the matrix comprised approximately circular-shaped pores (some as large as $15\ \mu\text{m}$ in dia.), Fig. 9a. Needles of coke usually about $10 \times 20\ \mu\text{m}$, see arrows in Fig. 9a, with a smooth surface were distributed with random orientation within the matrix. These were the finer ground coke particles (termed as flour) that was mixed with the binder during processing [32]. These elongated needles had a line marks along the long axes, and there were pores between these particles and the surrounding matrix, Fig. 9a. In addition, there are similar larger needle coke particle, for example $200 \times 500\ \mu\text{m}$ (one example of part of this type of particle is shown in Fig. 9b; a more complete image of this particle is shown later in Fig. 10a) that comprise long, thin and narrow ribbons. FIB milling across these particles revealed that clusters of these ribbons had ‘sintered’ to form a denser region, Fig. 9c.

FIB milling was undertaken at a location where a large filler particle joins the matrix, Fig. 9d. Four locations, sites 1 to 4, were investigated, Fig. 9d, and the number of small pores was reduced significantly compared with unirradiated material, Fig. 3. In addition, one notable feature for all these sections was the presence of a layer of material (from nano-metre to $\sim 3\ \mu\text{m}$ thick) with lighter contrast attached to the inner surface of the open pores as marked by arrows in Fig. 9d. This layer was not observed in any of the non-irradiated materials and is

possibly related to the radiolytic oxidation process. Radiolytic oxidation occurs when CO_2 is decomposed by ionising radiation to give reactive oxidising species. For Magnox reactors, hydrogen was added on a regular basis to avoid the carbon deposition. In general, radiolytic oxidation via CO_2 gas access to existing open pores removes material from the inner surface and would enlarge the pores to give the structures similar to those observed in Fig. 9a.

Micro-cantilever specimens were created in the dense regions within the filler particles and the matrix, respectively. Fig. 10a shows the loading probe positioned on a micro-cantilever milled at the end of a bundle of filler particle ribbons in the irradiated PGA. These cantilevers have the features of the interfaces on the surface, Fig. 10b, and these sites were where fracture eventually occurred. In total, three cantilevers were tested; the measured elastic moduli were 37.5 GPa, 48.6 GPa and 86.7 GPa, respectively; the corresponding flexural strengths derived were 652 MPa, 1080 MPa and 1340 MPa, respectively (Table II). A schematic of the orientation and flexural strength is shown in Fig. 10c. The ‘weakest’ cantilever was created normal to and tested parallel with the layers of ribbons, and the flexural strength was about 652 MPa. The highest strengths, 1080 MPa and 1340 MPa, were derived when a cantilever was positioned at 20 and 70 degree from the extrusion direction. For the three cantilever specimens tested, fractured locations were two to three micrometres from the root so that the measured strength is an evaluation of these defects and the ‘true’ strength of the flaw-free material within the filler particles should be higher than these values. For simplicity, the measurement of the micro-cantilevers in unirradiated PGA graphite are not described in detail. But as shown in Table II, the elastic modulus was lower than 20 GPa for both the particles and matrix, with the highest flexural strength less than 300 MPa. The elastic modulus increased by a factor of 2 to 4 in the irradiated filler particles compared with the unirradiated condition (Table II).

The load-displacement curves for these cantilevers typically comprised a linear range at low load that became progressively non-linear as the load approached fracture, Fig. 10d. After initiation, the cracks usually arrested at specific microstructural features. As a consequence, the load applied remained high to maintain stable crack propagation through the cross-sections of the test specimens. For example, the specimen tested in Fig. 10d had a crack mouth opening displacement of $0.18\text{ }\mu\text{m}$ while the load remained almost constant. Examination of the fractured surface of this cantilever revealed an irregular initial crack path, Fig. 10e, and the subsequent crack propagation surface had a complex geometry in 3D space

which contributed to the stable crack growth at higher loads. In addition, there were alternating nano-metre thickness lines with a darker contrast shown by the arrows embedded in the cantilever volume, Fig. 10e. These related to the interaction between graphite sheets in the particles arising from neutron irradiation, Fig. 10f.

In the matrix, two micro-cantilevers were created within the solid regions between large pores and when loaded both fractured at the root, Fig. 11a. The load-displacement curves for both specimens were similar and as shown in Fig. 11b. They typically comprised three stages: (i) linear-elastic up to 60 to 70% of the peak load; (ii) a plateau where the load remained almost constant while displacement extended by about 0.15 to 0.20 μm ; and (iii) a final stage with a lower slope to failure. Post peak load, a brittle abrupt fracture was usually observed, and the fractured surface is shown in Fig. 11c. Elastic moduli were 5.2 GPa and 8.6 GPa for the two specimens, and the corresponding flexural strengths are 154 MPa and 357 MPa, respectively. These moduli and strengths are much lower than those measured in both the unirradiated PGA graphite and irradiated filler particles. In addition, compared with the filler particles, the specimens in the matrix sampled a more uniform material with no obvious surface breaking defects. Finally, when compare with the load-displacement curves from unirradiated material, these post-service graphite specimens exhibit more ‘brittle’ fracture characteristics, i.e. abrupt failure with no obvious post-peak load drops.

4. Discussion

4.1 Micro-scale mechanical properties

The present micro-cantilever testing configuration falls within the broad category of ‘*in situ*’ single micro-scale cantilever tests. Of the range of carbonaceous materials selected, apart from the vitreous carbon, they contain varying amounts of sub micro-scale porosity together with pores at the macro-length scale. Hence, for many of the micro-scale cantilever beam tests variability in the measured data arises from sampling selected volumes of these heterogeneous materials. The advantage of these micro-cantilever beam tests is that it is possible (i) to evaluate the properties of the microstructural constituents of the polygranular graphites, (ii) to determine the ‘true’ properties of material that contains macro-scale pores and (iii) to undertake measurements on small volumes of irradiated material. Compared with the earlier geometry of the micro-cantilevers described by Darnbrough et al [19], using the present specimens it is possible to view the root region which allows both the location of fracture initiation to be observed over the full length of the specimen and measurement of the

loading arm length to be made more accurately. This provides improved confidence in the evaluated mechanical properties of these carbonaceous materials. However, it has to be recognised that the stress state at the specimen root is complex. For the present tests the majority of the failures did not occur at the root region mainly due to the presence of nano-scale pores and flaws in the materials. It would be more appropriate to use a tapered geometry that would allow the strain energy to be kept constant, but the difficulties associated with producing such specimen reproducibility offsets the advantages of adopting that geometry. In terms of the overall micro-scale properties, the measurements undertaken on the vitreous carbon provide a validation for the mechanical data derived from these micro-cantilever tests. As shown in Fig. 6, the elastic modulus E and strength obtained from vitreous carbon were reproducible between the tests within experimental scatter and they are consistent with the bulk value. Fig. 12a shows the correlation between E and the flexural strength for the vitreous carbon and PG25 filter graphite. The data show a simple, if scattered, correlation where $\sigma \sim (1/60)E$, which is comparable with other brittle materials such as ceramics and glassy carbon ($\sigma \sim (1/(10-100))E$) [33]. Fig. 12b includes all the measured data for the range of other materials considered and the data fit reasonably well with this relationship, apart from the large scatter in the IM1-24 material. This is consistent with the more quasi-brittle characteristics of the IM1-24 and PGA graphite arising from the presence of significant porosity at the sub-micro-length scale.

There are two factors that should be taken into account when comparing the micro- and macro-scale data. Firstly, for the three types of graphite, the values of flexural strength measured at micro-scale are much higher than those from the macro-scale, by an order of magnitude, compare Table II and Table I. The elastic moduli derived from the linear part of the loading curve, using IM1-24 graphite as an example, are mainly in a range between 10 to 30 GPa at micro-scale with values extending to 67 GPa. This is because the microstructure tested at these two length-scales is different since the micro-scale cantilever specimens include both micro-metre and sub-micro-metre porosity, while macro-scale specimens sample pores at both micro- and macro-length scales. Secondly, the broad distribution of the measured properties at the micro-scale is due to the varying pores, defects and the crystallographic orientation of the grains sampled in each cantilever volume. Again, at the macro-scale, the sampled volume has to contain a sufficient number of characteristic microstructural features to produce a representative quantification of the properties. Certainly, if the volume is too small, then larger scatter in the data is expected. Admittedly, the micro-

size specimens tested in the current work may not represent all aspects of the microstructure for the material. It is the *in situ* observation of the deformation and fracture and their correlation to the measured mechanical properties that are essential to ultimately develop a complete mechanistic understanding of the material. For example, without *in situ* micro-mechanical testing, the complex inter-locking microstructural contributions could be easily mis-interpreted.

It has been recognised that the measurements obtained at micro-scale provide the appropriate input parameters for computer models, in particular for the type of models based on the microstructure and the multi-phases [31][34][35]. The model proposed by Berre *et al* [34] derived the elastic modulus of the individual phase by extrapolating the measured phase density using X-ray tomography between pores (zero density with $E = 0$ GPa) and pore-free single crystal graphite (density = 2.26 g/cm^3 with $E = 19$ GPa). However, some of the E values measured by the micro-cantilevers in the current work (PG25, Gilsocarbon and PGA graphites) are higher than 19 GPa, which is the minimum E for single crystal graphite. This indicates that density is not the only factor affecting the E . The detailed microstructure including nano-scale crystallites and complex inter-locking architecture, Figs. 7, 9, 10, 11, could strengthen the material and lead to a higher modulus. As a consequence, micro-scale measurements provide the appropriate mechanical properties for the individual phases for use as input data to microstructure-based computer models and the macroscopic properties acts as the output and provide validation for the macro-scale predictions.

4.2 Crystallite size and orientation

The nano- and micro-scale pores, the size and orientation of graphite crystals and crystallites all potentially affect the measured properties of the cantilever specimens [36][37]. In general, the structure of heat-treated carbon is usually characterised in terms of the parameters, L_a and L_c , defined as the length and thickness of the graphite lamellae structure within the material, respectively [42]. A range of non-destructive techniques are available for such characterisation. For example, Raman spectroscopy provides information of the bond structure and type for graphite [38]. From the intensity ratio of the first order defect-related D peak and G peak which corresponds to a doubly degenerate phonon mode with E_{2g} symmetry for sp^2 bonds, the in-plane crystallite size can be determined using the Tuinstra-Koenig relationship [39]. The crystallite size can also be derived from XRD using the Scherrer line broadening formula. Usually, these two methods are combined and provide validation on the

measured crystallite size. For carbon materials prepared below 1000°C, these two parameters are usually around 1 nm indicating a relatively low graphitization level and high disordered structure [2]. With heat treatment up to 3000°C, these two parameters could reach values up to 100 nm via three thermally activated processes: in-plane crystallite growth (increase in L_a , while L_c and the number of crystallites remain constant), coalescence of a crystallites along the c-axis (increase in L_c and reduction in the number of crystallites), and coalescence of crystallites along the a-axis (increase in L_a and reduction in the number of crystallites) [40]. Typical measurements of these two parameters in PGA and IM1-24 graphites are listed in Table III.

Table III L_a and L_c measurements for PGA and IM1-24 graphites using Raman spectroscopy, XRD and transmission electron microscopy, respectively [36][41][42].

Graphite type	L_a	L_c	Methods [36, 41-42]
PGA (1.74 g/cm ³)	21±4 nm	-	Raman [36, 41]
IM1-24 (1.81 g/cm ³)	20±11 nm	-	
PGA (1.74 g/cm ³)	7-44 nm	-	Raman [42]
IM1-24 (1.81 g/cm ³)	10-35 nm	-	
PGA (1.74 g/cm ³)	44.8 nm	23.7 nm	XRD
IM1-24 (1.81 g/cm ³)	47.2 nm	35.6 nm	
PGA (1.74 g/cm ³)	5-80 nm	2-26 nm (10.3±7.4 nm)	TEM
IM1-24 (1.81 g/cm ³)	5-200 nm	2-36 nm (11.2±9.1 nm)	

It has been difficult to quantify the orientation of the crystallites in commercial graphites because the binder phase of nuclear graphite has a complex microstructure and the outcomes from the graphitizing process are not well understood. For example, PGA graphite binder contains various forms of carbon such as well-graphitized structures, quinoline insoluble particles, nano-sized graphite structures, chaotic structures and non-graphitizing carbon [32][43]. The various microstructures of the binder in nuclear graphites have been defined by distinguishing regions of common basal plane alignment extending over linear dimensions greater than 100 μm and those of small randomly oriented pseudo-crystallites with linear dimensions of common basal plane orientation of less than about 10 μm [35][43]. The micro-cantilever specimens used for the present evaluation of mechanical properties were of aspect ratio 5:1 with a side length of between 2 μm and 7 μm so that when a crack propagates, even neglecting the fact it follows a tortuous path, it would traverse $\sim 10^4$ crystallites for the smallest size of specimen tested. Since the microstructure for the polygranular commercial reactor core graphites are heterogeneous, then a selection of randomly oriented crystallites will be sampled within, but particularly between, specimens. As discussed above, it is the nano- and sub-micro pores and flaws that dominate the scatter in the measured data.

4.3 Failure modes

In terms of failure modes of nuclear graphite, such as PG25 filter graphite, IM1-24 and PGA, each displayed quasi-brittle fracture behaviour when tested at macro-scale [23]. At micro-scale, these characteristics were also present when a single crack formed, Figs. 7 to 11. The *in situ* cantilever loading is undertaken via displacement control, therefore, the local ligament fracture relates to a load drop in the load-displacement curves. In particular, an important observation is that the crack initiation site is not necessarily the site of final fracture, i.e. when damage was introduced or an existing micro-defect opened some of these features subsequently closed by relaxation of strain as a new crack was formed in the vicinity upon further loading. This phenomenon provides implications of the formation of micro-cracks at the macro-scale. Complexity of the microstructure and porosity is the key to promoting micro-cracks that are associated with the quasi-brittle characteristics of these graphites. Ultimately, micro-cracks nucleate and coalesce to form macro-cracks [44]. At the micro-scale, the formation of micro- and sub-micro-metre cracks is analogous to the macro-scale behaviour. However, one point worth noting is that the graphite materials (PG25, IM1-24 and PGA graphites) are more ductile at micro-scale compared with the reported macro-scale data - although the vitreous carbon displayed similar failure strain both at micro- and macro-scale. The failure strain of Gilsocarbon graphite has been reported to be less than 0.3% for macro-scale uniaxial tension test [45][34]. Whereas the failure strain measured in the present work is over twice the average value $\sim 0.6\%$ with a highest value of 1.0%. Combined with the investigation of the fractured surface, this ductility could be associated with basal slip leading to sliding of the graphite layers under load.

4.4 Neutron irradiation

When PGA graphite is exposed to fast neutron irradiation in the CO₂ gas service environment of a Magnox reactor, its mechanical properties change. These changes arise from two mechanisms: the first due to the injection of lattice point defects which increase both the elastic modulus and the fracture strength; the second arises from radiolytic oxidation which reduces both of these properties due to mass loss which results in the formation of pores. As a consequence, the overall change in these properties is the result of a competition between neutron irradiation hardening and oxidation weakening [6][46][41][47]. The micro-scale cantilever beam tests have specific advantages when testing this irradiated PGA graphite because mechanical properties can be measured on both the filler particles and the matrix. However, there is the potential that the measured mechanical properties at this micro-length-

scale could be influenced by the size, orientation and distribution of the complex crystallite substructure within both the filler particles and the matrix. As indicated in Section 4.3, such contributions associated with the crystallites are not easily evaluated. But since their size is typically of the order of 10 nm dia., the micro-scale cantilever test specimens sample many crystallites and therefore provide an average value that accommodates any local crystallite contribution to the measured mechanical properties.

For the filler particles, as shown in Table II, despite the scatter in the data, there is a significant increase in both the elastic modulus from an average value of 20 GPa to 55 GPa and for the fracture strength from 300 MPa to 1024 MPa on average for a neutron irradiation of 33.2×10^{20} DIDO equivalent dose. Therefore, the particles indeed follow the increases in properties typically attributed to fast neutron hardening. However, surprisingly, the elastic modulus for the matrix reduced to an average of 6.9 GPa and 255 MPa for the average fracture stress. Although there is not a simple explanation for the changes to the matrix, it has been noted by other workers that the mass loss during neutron irradiation occurs preferentially within the matrix [4][43]. Hence the changes observed within the matrix probably relate to a complex, but unspecified, interaction between the irradiation induced damage and the oxidation mechanism.

To test the significance of these micro-scale test data for both unirradiated and irradiated PGA graphite, the values described in this paper have been used as inputs to a microstructurally based, multi-scale computer model [31]. The computer modelling was designed to predict at the macro-length-scale the load-displacement response and the deformation and fracture properties for material containing macro-porosity arising from fabrication in unirradiated material and neutron dose in an irradiated oxidising environment [31]. Using the mean values given in Table II, both the magnitude and trend predicted for the elastic modulus and fracture strength were in reasonable agreement with experimentally measured values obtained at the macro-length-scale from bend geometry tests. Thus there is consistency between the experimental observations and model predictions when using the micro-scale mechanical property data.

5. Conclusions

In situ micro-mechanical testing has been adopted to evaluate the local mechanical properties of four different types of carbonaceous materials: vitreous carbon, filter graphite, IM1-24 graphite, unirradiated and irradiated PGA graphite. The key outcomes are:

- It is demonstrated that cantilever beam test specimens can be prepared from (i) samples of complex geometry, e.g. foams; (ii) specific locations within the overall microstructure and (iii) small volumes of irradiated material.
- The micro-scale mechanical properties of vitreous carbon have values of elastic modulus, fracture strength and strain to failure comparable with data obtained from bulk samples and therefore validate the micro-scale measurements. Moreover, the brittle fracture characteristics were similar to macro-scale material.
- Filter graphite, IM1-24 and PGA graphites, which contained micro-scale porosity all showed a much higher elastic modulus and flexural strength compared with macro-scale because contributions from macro-pores have been removed. At micro-scale, the cantilever specimens usually show progressive fracture within the local microstructure.
- Filler particles and matrix in PGA graphite response differently to neutron irradiation and radiolytic oxidation. The filler particles become stiffer and stronger whereas matrix becomes more compliant. But both demonstrated a more brittle fracture mode compared with unirradiated specimens.
- Micro-mechanical tests of the type described provide a powerful method for evaluating individual features of carbonaceous materials where the microstructure is complex. These tests enable fracture characteristics of the various regions to be explored. Despite the advantage of the *in situ* micro-mechanical testing on the investigation of local mechanical-microstructure relationship, the variation of local features result in a broad distribution of the measured data.

Acknowledgement

The authors acknowledge the ESPRC grant: EP/J019801/1 (QUBE: QUasi-Brittle fracture: a 3D Experimentally-validated approach) and EDF Energy Ltd for funding. DL acknowledges the EPSRC postdoctoral fellowship grant: EP/N004493/1 (An innovative, multi-scale, real-time approach to the understanding of deformation and fracture in irradiated nuclear reactor core graphites) and the Royal Commission for the Exhibition of 1851 Research Fellowship Scheme. The authors thank Dr Peter Heard and Dr Keith Hallam (University of Bristol) for helpful and valuable discussions.

References

- [1] F.C. Cowlard, J.C. Lewis, Vitreous carbon - A new form of carbon, *J. Mater. Sci.* 2 (1967) 507–512.
- [2] P.J.F. Harris, Structure of non-graphitising carbons, *Int. Mater. Rev.* 42 (1997) 206–218.
- [3] R.O. Ritchie, Fatigue and fracture of pyrolytic carbon: a damage- tolerant approach to structural integrity and life prediction in “ceramic” heart valve prostheses, *J. Heart Valve Dis.* 5 Suppl 1 (1996) S9–31.
- [4] A. Hodgkins, T.J. Marrow, M.R. Wootton, R. Moskovic, P.E.J. Flewitt, Fracture behaviour of radiolytically oxidised reactor core graphites: a view, *Mater. Sci. Technol.* 26 (2010) 899–907.
- [5] D.E. Baker, Graphite as a neutron moderator and reflector material, *Nucl. Eng. Des.* 14 (1971) 413–444.
- [6] J.E. Brocklehurst, B.T. Kelly, Analysis of the dimensional changes and structural changes in polycrystalline graphite under fast neutron irradiation, *Carbon.* 31 (1993) 155–178.
- [7] A.P.G. Rose, D.D. Jones, The mechanical properties of irradiated pitchcoke graphite, *Carbon.* 24 (1986) 521–526.
- [8] V.T. Srikar, S.M. Spearing, A critical review of microscale mechanical testing methods used in the design of microelectromechanical systems, *Exp. Mech.* 43 (2003) 238–247.
- [9] M. Hopcroft, T. Kramer, G. Kim, K. Takashima, Y. Higo, D. Moore, Micromechanical testing of SU-8 cantilevers, *Fatigue & Fract. Eng. Mater. Struct.* 28 (2005) 735–742.
- [10] B.N. Jaya, C. Kirchlechner, G. Dehm, Can microscale fracture tests provide reliable fracture toughness values? A case study in silicon, *J. Mater. Res.* 30 (2015) 686–698.
- [11] D.E.J. Armstrong, A.J. Wilkinson, S.G. Roberts, Measuring anisotropy in Young’s modulus of copper using microcantilever testing, *J. Mater. Res.* 24 (2011) 3268–3276.
- [12] K. Matoy, H. Schönherr, T. Detzel, T. Schöberl, R. Pippan, C. Motz, et al., A comparative micro-cantilever study of the mechanical behavior of silicon based passivation films, *Thin Solid Films.* 518 (2009) 247–256.
- [13] T.P. Weihs, S. Hong, J.C. Bravman, W.D. Nix, Mechanical deflection of cantilever microbeams: A new technique for testing the mechanical properties of thin films, *J. Mater. Res.* 3 (2011) 931–942.
- [14] D.E.J. Armstrong, X. Yi, E.A. Marquis, S.G. Roberts, Hardening of self ion implanted tungsten and tungsten 5-wt% rhenium, *J. Nucl. Mater.* 432 (2013) 428–436.
- [15] D.E.J. Armstrong, A.S.M.A. Haseeb, S.G. Roberts, A.J. Wilkinson, K. Bade, Nanoindentation and micro-mechanical fracture toughness of electrodeposited nanocrystalline Ni–W alloy films, *Thin Solid Films.* 520 (2012) 4369–4372.
- [16] J.A.J. van der Rijt, K.O. van der Werf, M.L. Bennink, P.J. Dijkstra, J. Feijen, Micromechanical testing of individual collagen fibrils., *Macromol. Biosci.* 6 (2006) 697–702.
- [17] S. Fazluddin, Crack growth resistance in nuclear graphite, (2002). PhD thesis, University of Leeds.
- [18] D. Kiener, C. Motz, G. Dehm, Dislocation-induced crystal rotations in micro-compressed single crystal copper columns, *J. Mater. Sci.* 43 (2008) 2503–2506.
- [19] J.E. Darnbrough, D. Liu, P.E.J. Flewitt, Micro-scale testing of ductile and brittle cantilever beam specimens in situ with a dual beam workstation, *Meas. Sci. Technol.* 24 (2013) 055010.
- [20] N.C. Gallego, J.W. Klett, Carbon foams for thermal management, *Carbon.* 41 (2003) 1461–1466.
- [21] R. Taylor, R.G. Brown, K. Gilchrist, E. Hall, A.T. Hodds, B.T. Kelly, et al., The

- mechanical properties of reactor graphite, *Carbon*. 5 (1967) 519–531.
- [22] P.J. Heard, M.R. Wootton, R. Moskovic, P.E.J. Flewitt, Crack initiation and propagation in pile grade A (PGA) reactor core graphite under a range of loading conditions, *J. Nucl. Mater.* 401 (2010) 71–77.
- [23] D. Liu, P. Heard, S. Nakhodchi, P. Flewitt, Graphite Testing for Nuclear Applications: The Significance of Test Specimen Volume and Geometry and the Statistical Significance of Test Specimen Population, ASTM International, 100 Barr Harbor Drive, PO Box C700, West Conshohocken, PA 19428-2959, 2014.
- [24] J.S. Field, M. V. Swain, The indentation characterisation of the mechanical properties of various carbon materials: Glassy carbon, coke and pyrolytic graphite, *Carbon*. 34 (1996) 1357–1366.
- [25] N. Iwashita, J.S. Field, N. V Swain, Indentation hysteresis of glassy carbon materials, *Philos. Mag. a-Physics Condens. Matter Struct. Defects Mech. Prop.* 82 (2002) 1873–1881.
- [26] N. Iwashita, M. V. Swain, J.S. Field, N. Ohta, S. Bitoh, Elasto-plastic deformation of glass-like carbons heat-treated at different temperatures, *Carbon*. 39 (2001) 1525–1532.
- [27] P. Diss, J. Lamon, L. Carpentier, J. Loubet, P. Kapsa, Sharp indentation behavior of carbon/carbon composites and varieties of carbon, *Carbon*. 40 (2002) 2567–2579.
- [28] C. Garion, Mechanical Properties for Reliability Analysis of Structures in Glassy Carbon, *World J. Mech.* (2014) 79–89.
- [29] D. Liu, H. Sun, J.W. Pomeroy, D. Francis, F. Faili, D.J. Twitchen, et al., GaN-on-diamond electronic device reliability: Mechanical and thermo-mechanical integrity, *Appl. Phys. Lett.* 107 (2015) 251902.
- [30] B.D. Ratner, A.S. Hoffman, F.J. Schoen, J.E. Lemons, *Biomaterials Science: An Introduction to Materials in Medicine*, Academic Press, 2012.
- [31] B. Šavija, D. Liu, G. Smith, K.R. Hallam, E. Schlangen, P.E. Flewitt, Experimentally informed multi-scale modelling of mechanical properties of quasi-brittle nuclear graphite, *Eng. Fract. Mech.* 153 (2015) 360–377.
- [32] K.Y. Wen, T.J. Marrow, B.J. Marsden, The microstructure of nuclear graphite binders, *Carbon*. 46 (2008) 62–71.
- [33] C.C. Yuan, X.K. Xi, On the correlation of Young's modulus and the fracture strength of metallic glasses, *J. Appl. Phys.* 109 (2011) 033515.
- [34] C. Berre, S.L. Fok, B.J. Marsden, P.M. Mummery, T.J. Marrow, G.B. Neighbour, Microstructural modelling of nuclear graphite using multi-phase models, *J. Nucl. Mater.* 380 (2008) 46–58.
- [35] T.D. Burchell, A microstructurally based fracture model for polygranular graphites, *Carbon*. 34 (1996) 297–316.
- [36] B.E. Mironov, A.V.K. Westwood, A.J. Scott, R. Brydson, A.N. Jones, Structure of different grades of nuclear graphite, *J. Phys. Conf. Ser.* 371 (2012) 012017.
- [37] A.N. Jones, G.N. Hall, M. Joyce, A. Hodgkins, K. Wen, T.J. Marrow, et al., Microstructural characterisation of nuclear grade graphite, *J. Nucl. Mater.* 381 (2008) 152–157.
- [38] T. Tanabe, K. Niwase, N. Tsukuda, E. Kuramoto, On the characterization of graphite, *J. Nucl. Mater.* 191-194 (1992) 330–334.
- [39] F. Tuinstra, Raman Spectrum of Graphite, *J. Chem. Phys.* 53 (1970) 1126.
- [40] F.G. Emmerich, Evolution with heat treatment of crystallinity in carbons, *Carbon*. 33 (1995) 1709–1715.
- [41] B.E. Mironov, H.M. Freeman, A.P. Brown, F.S. Hage, A.J. Scott, A.V.K. Westwood, et al., Electron irradiation of nuclear graphite studied by transmission electron microscopy and electron energy loss spectroscopy, *Carbon*. 83 (2015) 106–117.

- [42] G.B. Neighbour, ed., *Modelling and Measuring Reactor Core Graphite Properties and Performance*, Royal Society of Chemistry, Cambridge, 2012.
- [43] P.J. Hacker, G.B. Neighbour, B. McEnaney, The coefficient of thermal expansion of nuclear graphite with increasing thermal oxidation, *J. Phys. D. Appl. Phys.* 33 (2000) 991–998.
- [44] M.R. Joyce, T.J. Marrow, P. Mummery, B.J. Marsden, Observation of microstructure deformation and damage in nuclear graphite, *Eng. Fract. Mech.* 75 (2008) 3633–3645.
- [45] S. Yoda, M. Eto, T. Oku, Change in dynamic young's modulus of nuclear-grade isotropic graphite during tensile and compressive stressing, *J. Nucl. Mater.* 119 (1983) 278–283.
- [46] M.I. Heggie, I. Suarez-Martinez, C. Davidson, G. Haffenden, Buckle, ruck and tuck: A proposed new model for the response of graphite to neutron irradiation, *J. Nucl. Mater.* 413 (2011) 150–155.
- [47] P.A. Thrower, W.N. Reynolds, Microstructural changes in neutron-irradiated graphite, *J. Nucl. Mater.* 8 (1963) 221–226.

Table II The geometry, elastic modulus and flexural strength of all the cantilevers tested

Materials	Geometry (μm)	Elastic modulus (GPa)	Flexural
-----------	----------------------------	-----------------------	----------

			strength (MPa) ± 5%
Vitreous carbon	1.75×1.75×11.50	30.5	393
	1.25×1.25×8.80	25.8	295
	2.00×2.00×17.00	34.7	447
	3.25×3.25×21.00	25.0 (Load1); 25.4 (Load2)	283
PG25	1.80×1.80×10.00	16.2	261
	2.00×2.00×12.00	11.1	285
	2.50×2.50×20.00	25.4	524
	3.00×3.00×25.00	31.5 (Load1); 20.9 (Load2)	201
	3.20×3.20×20.00	34.8	604
	5.00×5.00×44.00	26.6	341
	6.60×6.60×44.00	18.0	192
IM1-24 graphite	1.00×1.00×5.00	7.7(Load1); 8.9(Load2); 8.4(Load3); 9.5(Load4)	423
	2.00×2.00×10.00	17.98 (Load1); 23.99 (Load2); 17.72(Load3); 36.435 (Load4); 18.0 (Load5)	564
	2.10×2.10×10.50	27.63 (Load1); 22.07 (Load2)	611
	2.30×2.30×13.10	7.7 (Load1); 8.7 (Load2); 8.97 (Load3); 8.4 (Load4)	308
	1.40×1.40×11.00	25.2 (Load1); 19.1 (Load2); 18.6 (Load3); 16.4 (Load4); 17.8 (Load5); 17.1 (Load6)	979
	4.00×4.00×23.30	8.5 (Load1); 7.6 (Load2); 7.8 (Load3)	73
	2.30×2.30×18.10	5.8	84
	2.90×2.90×25.40	62.7 (Load1); 62.5 (Load2); 67.1 (Load3)	984
PGA unirradiated	2.50×2.50×14.00	16.5 (Load1); 17.1 (Load2); 15.9 (Load3)	264
	2.60×2.60×14.50	22.4	335
PGA_particle	2.30×2.30×11.80	37.5	652
Irradiated	2.80×2.80×16.10	79.4 (Load1); 86.7 (Load2)	1080
	2.30×2.30×14.00	48.6	1340
PGA_matrix	2.00×2.00×18.00	5.2	154
Irradiated	2.00×2.00×12.00	8.6	357

FIGURES

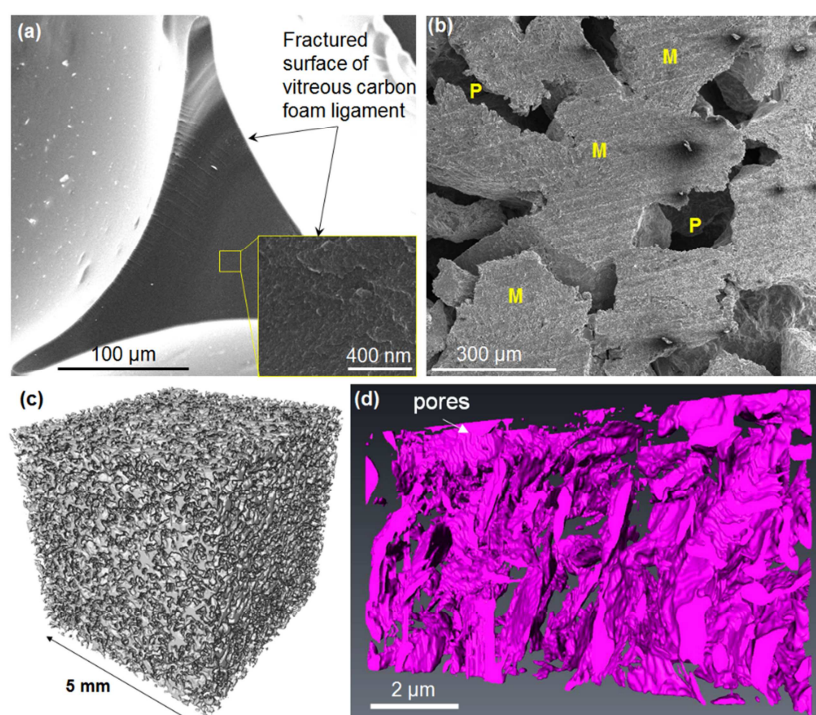


Fig. 1 Scanning electron microscopy (SEM) images of (a) vitreous carbon fractured surface and no obvious pores or texture observed; (b) surface of PG25 graphite - M: matrix, P: macro-pores; (c) the reconstructed tomographic images for a volume of PG25 graphite $5 \times 5 \times 5$ mm and (d) a 3D reconstructed pore structure of PG25 graphite obtained by focus ion beam serial milling.

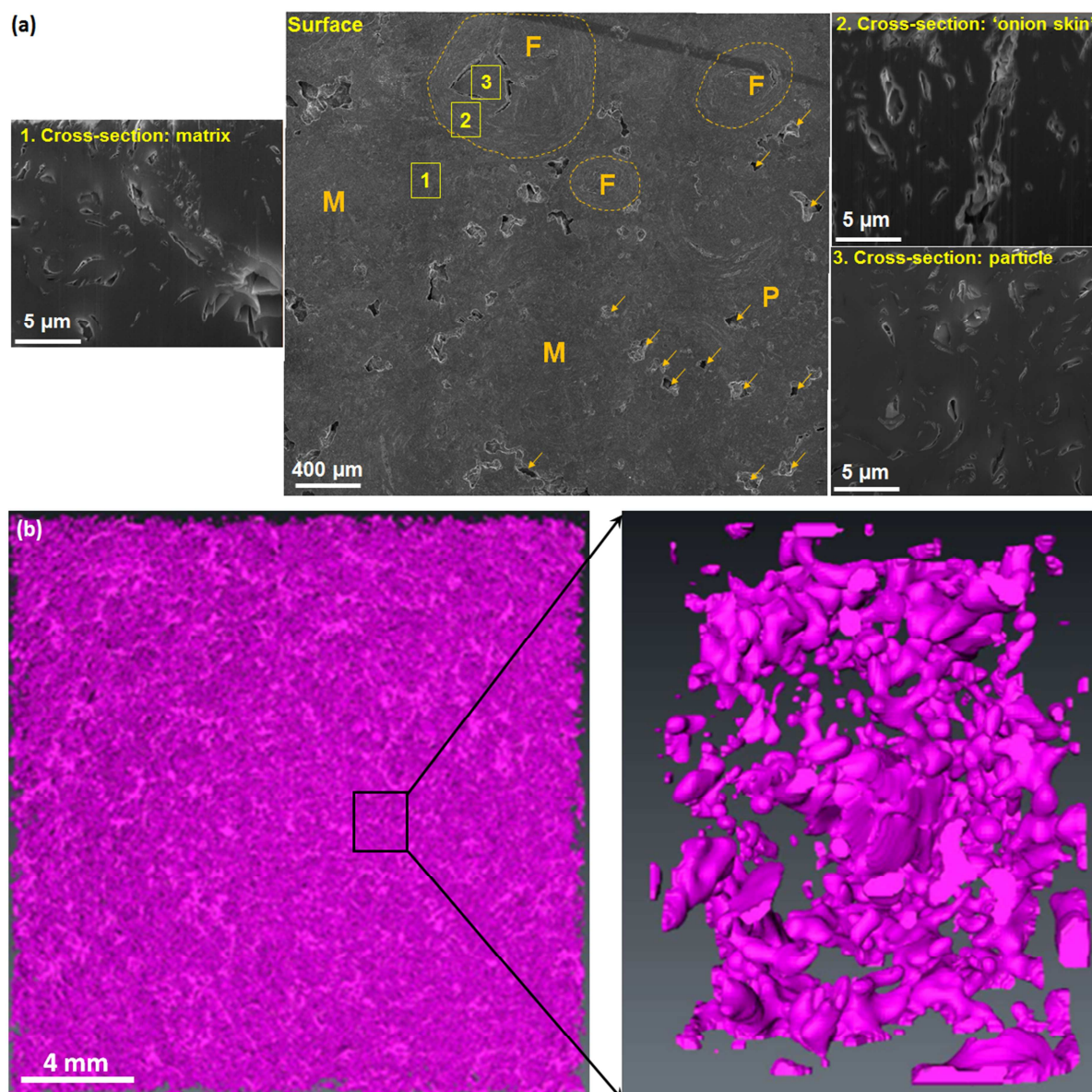


Fig. 2 (a) SEM image of Gilsocarbon IM1-24 grade graphite. M: matrix, F: filler particles (circled by dashed lines), P: macro-pores (marked by arrows – only part of the pores are marked to leave the other part original for a better view of the microstructure). High resolution FIB serial milling revealed the micro-pores in the cross-sections of the three constituent elements (1. matrix, 2. outer surface (onion skin) of filler particles, and 3. inside a filler particle), respectively; (b) reconstructed 3D pore structure together with detailed image of the marked region.

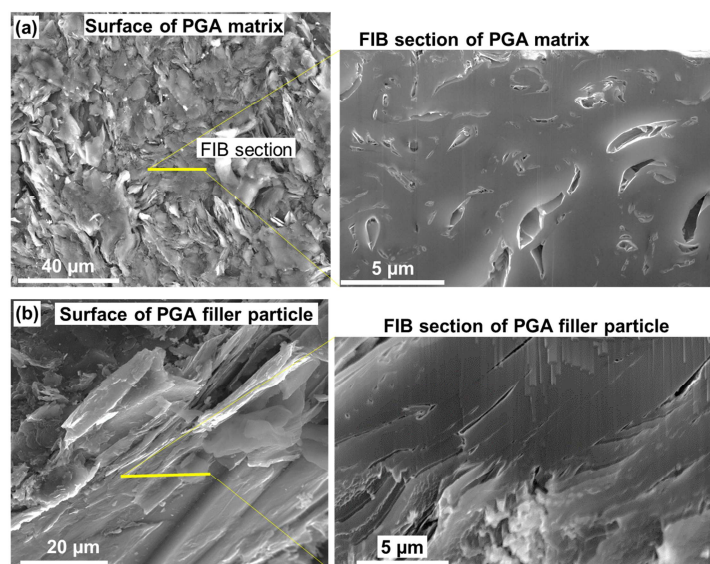


Fig. 3 (a) SEM image showing the surface of PGA graphite matrix. The insert shows the FIB cross-section with micro-scale pores; (b) a typical PGA filler particle with the insert showing the FIB cross-section with oriented pores within a particle.

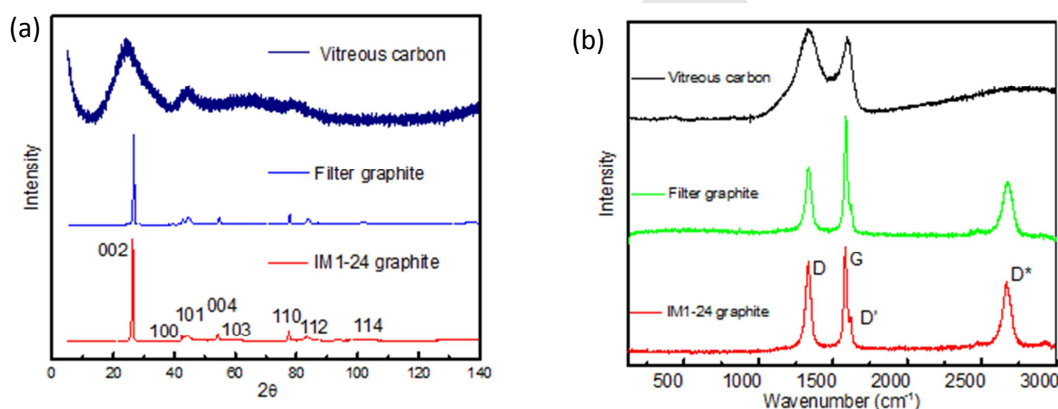


Fig. 4 (a) XRD patterns and (b) Raman spectra for vitreous carbon, filter graphite and Gilsocarbon graphite where G peak corresponds to a doubly degenerated phonon mode with E_{2g} symmetry, D and D' represent the disorder component and D* is the second order peak related to disorder

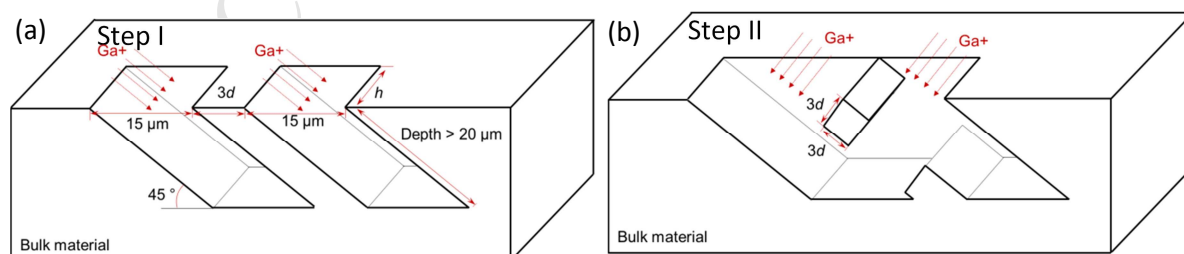


Fig. 5 Schematic showing the two main steps, (a) Step I and (b) Step II, for the milling of micro-cantilevers.

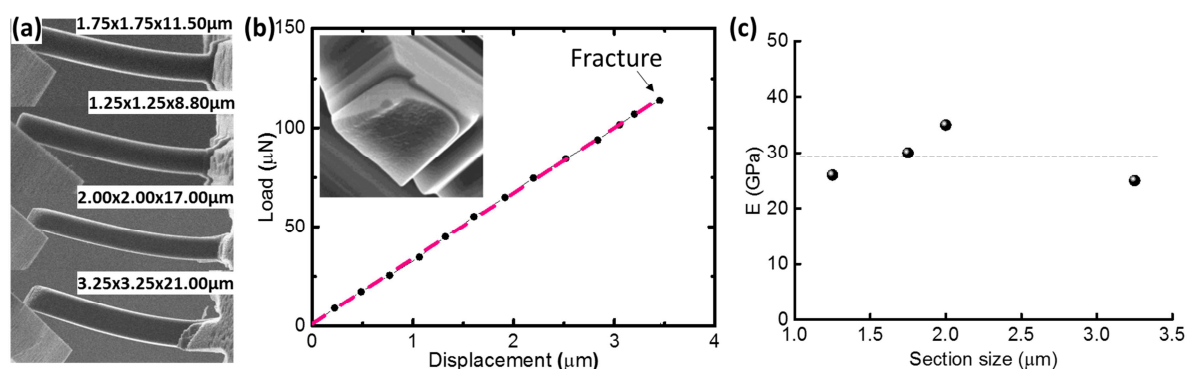


Fig. 6 (a) The deformation of the vitreous carbon cantilever beams prior to final fracture; (b) All the test specimens showed linear elastic deformation prior to an abrupt fracture (the load-displacement curve is from the $2.00 \times 2.00 \times 17.00 \mu\text{m}$ specimen in Table II) - the insert is a typical fracture surface of cantilever; (c) the elastic modulus does not display a systematic change with section size of the specimens, the average value is $29.0 \pm 4.5 \text{ GPa}$.

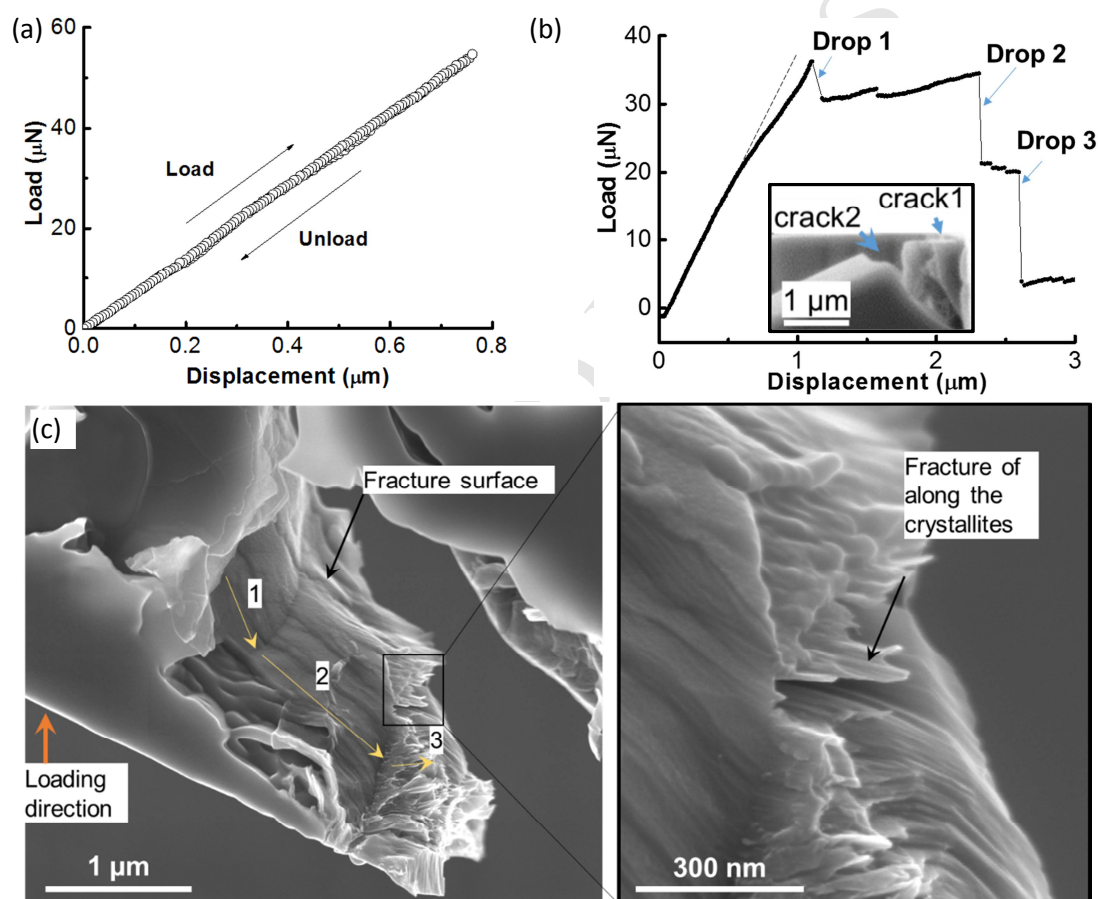


Fig. 7 For cantilever specimens made in filter graphite PG25: (a) under low load, a linear-elastic loading curve was usually observed ($3.00 \times 3.00 \times 25.00 \mu\text{m}$ specimen in Table II); (b) a load-displacement curve of the insert cantilever ($2.00 \times 2.00 \times 12.00 \mu\text{m}$ specimen in Table II) showing the formation of cracks accompanied with the load drops (loading direction from top to bottom); (c) fractured surface of a cantilever being loaded from bottom to top illustrates complex morphology of the fracture surface at the micro-scale; the selected region shows detail of the deflected crack path and the fracture along crystallite interface.

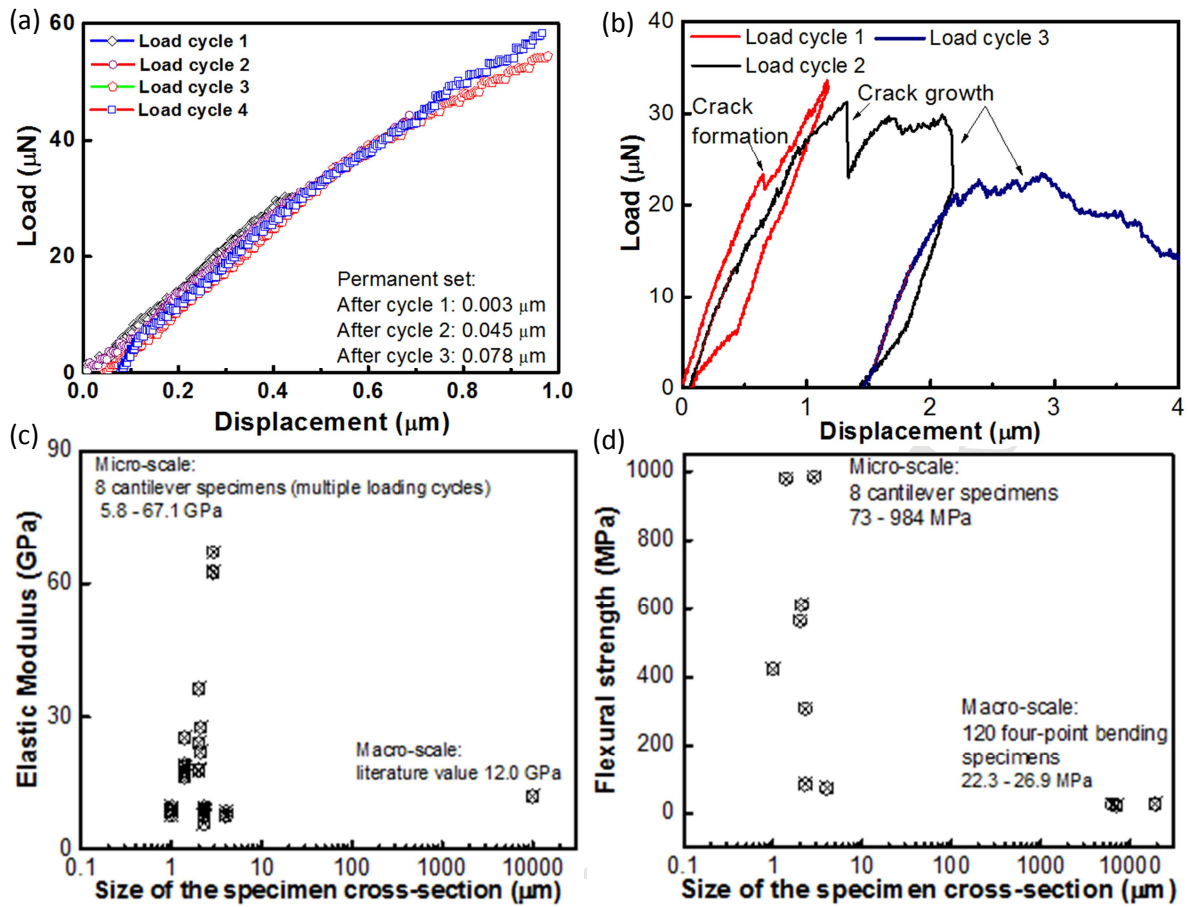


Fig. 8 For IM1-24 graphite: (a) the first four loading cycles for a cantilever sample showing the residual displacement ($2.30 \times 2.30 \times 13.10 \mu\text{m}$ specimen in Table II); (b) three loading cycles for a cantilever with existing complex surface defect ($4.00 \times 4.00 \times 23.30 \mu\text{m}$ specimen in Table II); (c) the elastic modulus and (d) the flexural strength measured at micro-scale compared with macro-scale literature values (Table I); errors bars are represented by the size of the symbols.

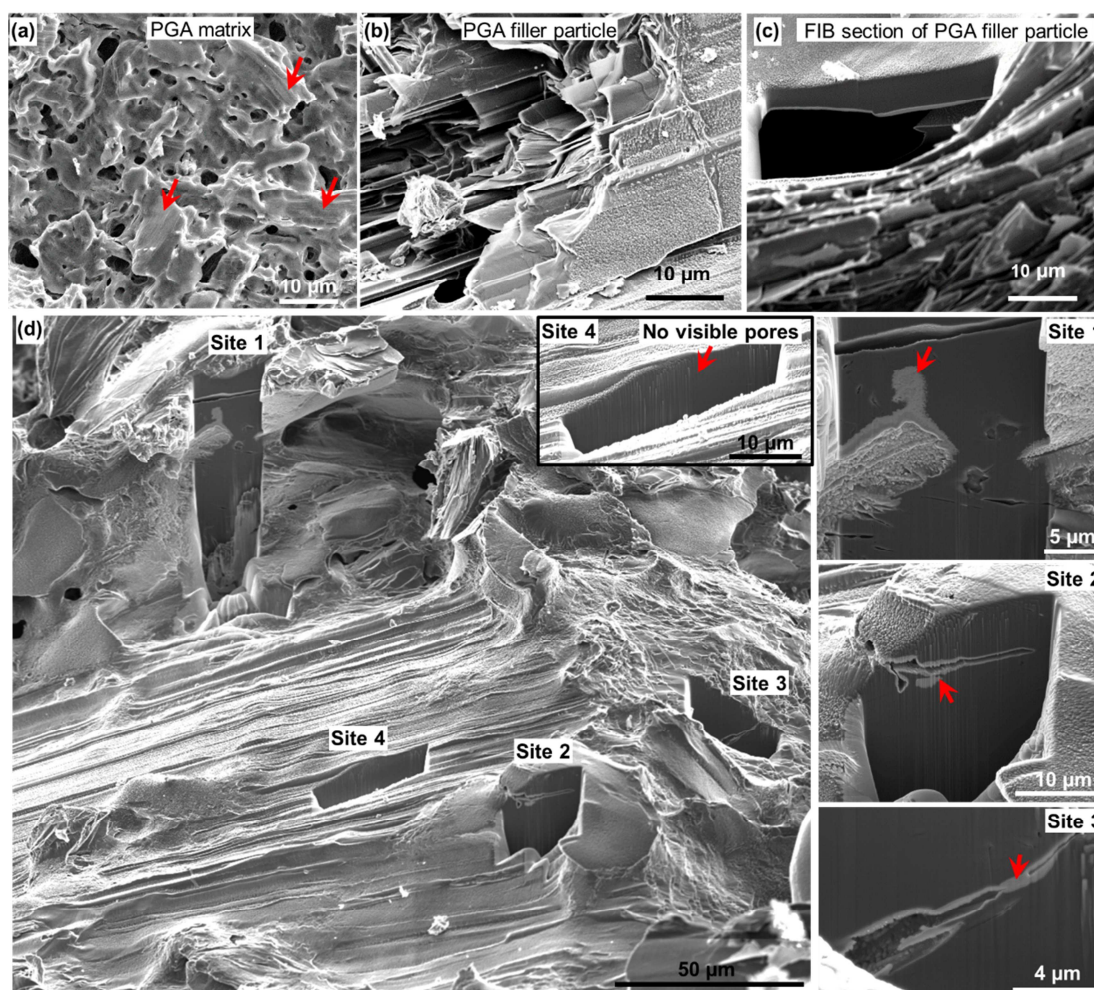


Fig. 9 SEM images of (a) surface of the irradiated and oxidised PGA graphite matrix; (b) PGA graphite filler particles with ribbon-shaped structure; (c) FIB cross-sections within a filler particle shows a cluster of the filler particle layers sintered together to form a denser region and left a large open pore next to it; (c) the enlarged open pores and flour of ground filler particles in irradiated PGA graphite matrix; (d) a large filler particle embedded in the matrix showing the four sites selected for FIB cross-section imaging; a higher magnification of sites 1 to 4 show the sintered micrometre pores in the 'dense' region and the dominating large pores.

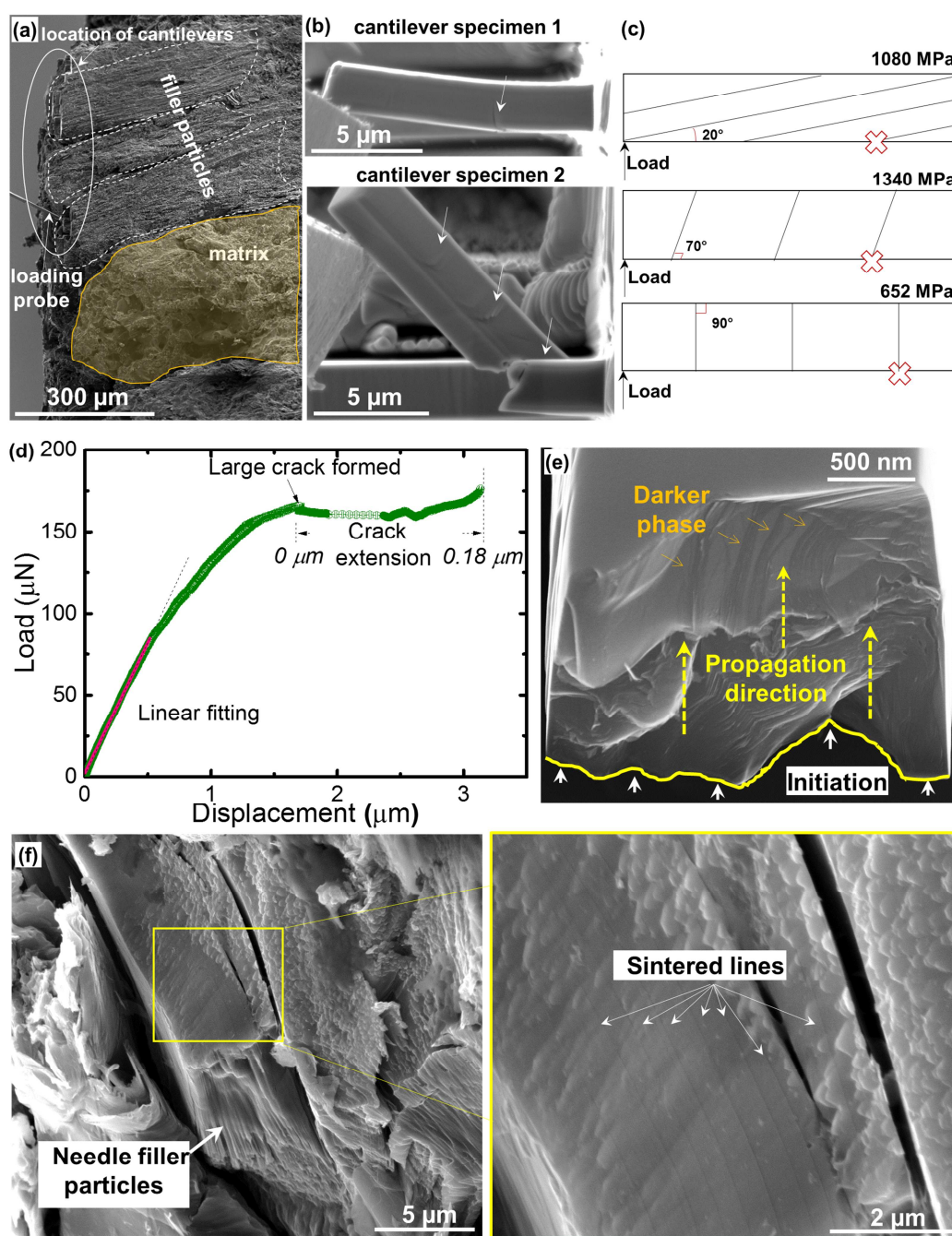


Fig. 10 For irradiated and radiolytically oxidised PGA graphite filler particle: (a) an overview of the probe in place to load micro-cantilever beam specimens created on the edge of a bundle of filler particle ribbons (filler particles are circled by dashed lines; matrix is the adjacent shaded area); (b) two typical example micro-cantilevers in filler particles. The elongation direction of the particles intersect with the cantilevers resulted in oriented interfaces visible on the cantilever surface; (c) three cantilevers created with different relative orientation with the long axis of the filler particles had different flexural strength values; (d) a typical loading curve showing the linear, non-linear and post-peak macro-crack propagation stage when the load remained above 150 μN as the crack mouth opening displacement increased from 0 to 0.18 μm ; (e) fractography analysis of the fractured surface of cantilever 1 in (b) shows the tortuous initial crack path and undulating crack surface in a 3D space; (f) a typical example of the sintered boundaries between ribbons within a large filler particle.

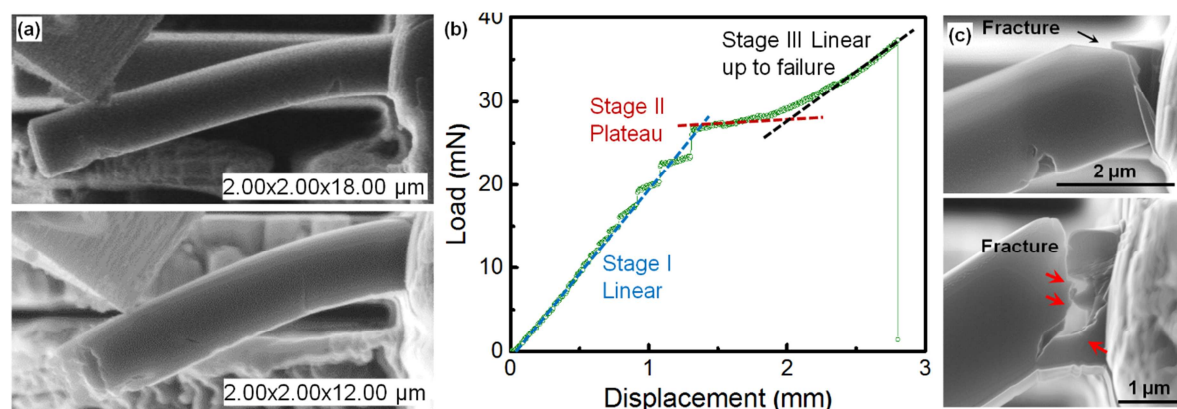


Fig. 11 For irradiated and radiolytically oxidised PGA graphite matrix: (a) deformed cantilever beam specimens prior to fracture (dimensions are $2.00 \times 2.00 \times 18.00 \mu\text{m}$ and $2.00 \times 2.00 \times 12.00 \mu\text{m}$ respectively); (b) the load-displacement curve for the $2.00 \times 2.00 \times 18.00 \mu\text{m}$ cantilever showing three stages: linear-elastic, plateau region and linear increase to fracture; (c) examination of the fractured surface at the root of the two cantilevers indicates a complex cross-sectional geometry.

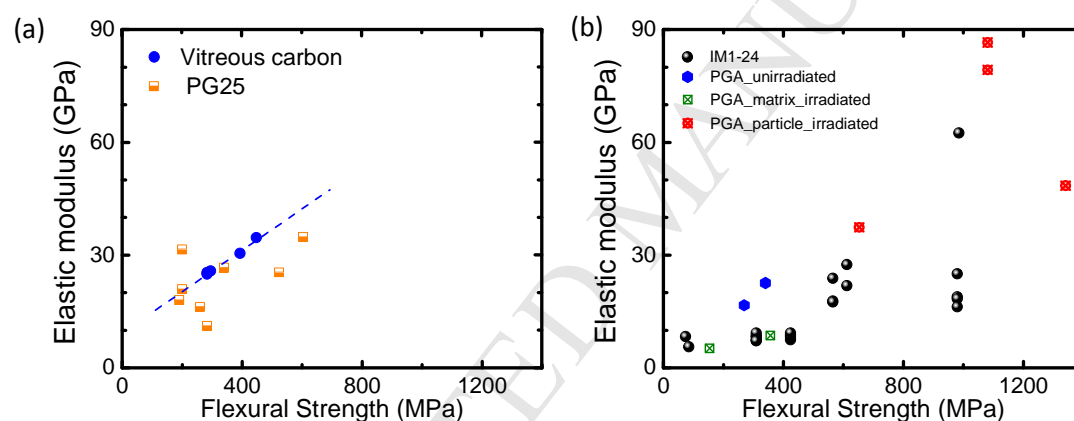


Fig. 12 The correlation between elastic modulus and flexural strength for (a) vitreous carbon and PG25 graphite and (b) IM1-24 and PGA graphites.